SANDIA REPORT
SAND2007-8100
Unlimited Release
Printed December 2007

MEMS Solar Energy Harvesting

Gregory N. Nielson, Jonathan Wittwer, Leslie Phinney, David Epp, Uma Krishnamoorthy, Vipin Gupta, and Paul Resnick

Prepared by
Sandia National Laboratories
Albuquerque, New Mexico 87185 and Livermore, California 94550

Sandia is a multiprogram laboratory operated by Sandia Corporation,
a Lockheed Martin Company, for the United States Department of Energy's
National Nuclear Security Administration under Contract DE-AC04-94AL85000.

Issued by Sandia National Laboratories, operated for the United States Department of Energy by Sandia Corporation.

Available to DOE and DOE contractors from
U.S. Department of Energy
Office of Scientific and Technical Information
P.O. Box 62
Oak Ridge, TN 37831

Telephone: (865) 576-8401
Facsimile: (865) 576-5728
E-Mail: reports@adonis.osti.gov
Online ordering: http://www.osti.gov/bridge

Available to the public from
U.S. Department of Commerce
National Technical Information Service
5285 Port Royal Rd.
Springfield, VA 22161

Telephone: (800) 553-6847
Facsimile: (703) 605-6900
E-Mail: orders@ntis.fedworld.gov
Online order: http://www.ntis.gov/help/ordermethods.asp?loc=7-4-0#online

SAND2007-8100
Unlimited Release
Printed December 2007

MEMS Solar Energy Harvesting

Gregory N. Nielson[1], Jonathan Wittwer[2], Leslie Phinney[3], David Epp[4], Uma Krishnamoorthy[1], Vipin Gupta[5], Paul Resnick[2]

[1]Advanced MEMS
[2]MEMS Core Technologies
[3]Microscale Science and Technology
[4]Applied Mechanics Development
[5]Solar Technologies

Sandia National Laboratories
P.O. Box 5800
Albuquerque, NM 87185-1080

Abstract

We have performed a preliminary investigation of a new approach for generating electrical power with solar energy that does not rely on the photovoltaic effect. This approach takes advantage of a unique interaction between a mechanically resonant device and optical illumination. The optical illumination is required to be a plane wave but does not require optical coherence which other reported optically excited mechanical resonant devices have required. The preliminary investigation described in this report included both experimental demonstration of key portions of the energy conversion process and FEA simulations to better understand the dependencies of this approach. This report also describes possible future areas of research.

Acknowledgements

The authors would like to acknowledge the MDL staff whose contribution to the fabrication of the MEMS devices was crucial to the success of the project.

This project was supported by Laboratory Directed Research and Development, Sandia National Laboratories, U.S. Department of Energy, under contract DE-AC04-94AL85000, as LDRD Project Number 115235, “MEMS Solar Energy Harvesting”. The selection for funding by the Seniors’ Council Tier 1 Investment Area is gratefully acknowledged.

Table of Contents

Executive Summary…….6

1.0 Introduction and Technical Description.……6

2.0 MEMS Design and Fabrication…….8

3.0 Experimental Results……...11

4.0 MEMS Photocell FEA Simulation and Analysis…….19

5.0 Summary and Future Work.…….28

References……..29

Executive Summary

In this report we describe and explore a completely new approach for solar energy harvesting that has the potential to provide solar energy at lower costs than current photovoltaic (PV) based solar power systems. This approach was inspired from previous Sandia research where MEMS devices were caused to resonate by laser (coherent) illumination. We use a similar interaction that we have conceived that will cause mechanical resonance with illumination by solar (i.e. incoherent, broad-spectrum) light. The energy stored in the mechanical resonance can be converted to electrical power through piezoelectric, capacitive, or other conversion processes. The cost reduction relative to PV technology results from the ability to use inexpensive materials rather than expensive semiconductor materials required by PV cells. In addition, the electric power generated can be 60 Hz AC, thus eliminating the power inverters required by grid-tied, PV power systems.

We describe in this report the first experimental demonstration of the new optical technique that does not require the coupling of an optical resonator to the mechanical resonator to achieve resonant mechanical motion. Because this technique does not use an optical cavity, the light used to drive the system does not have to be coherent (although for simplicity, we use coherent light for the testing of the device). In addition to the experimental work, we also describe a finite element model that captured the conversion of power from the optical domain to the mechanical domain. While further work is necessary, both the experimentation and the finite element modeling produced encouraging results.

1.0 Introduction and Technical Description

Developing cheap, renewable, non-polluting energy is arguably the greatest challenge facing society. Solar energy offers clean, renewable energy; however, power produced with photovoltaic (PV) solar cells is currently about four times the cost of power from conventional energy sources. In addition, efficiency improvements in PV technology have become incremental.

In this project, we have explored a radically new approach to solar energy harvesting. This approach uses an effect where optical illumination induces mechanical resonance in micromechanical structures [1]. The solar energy that is converted to mechanical energy in this way can then be converted to electrical power by either piezoelectric or capacitive means, similar to MEMS vibrational energy harvesters that convert ambient mechanical vibrations to electrical energy [2, 3]. The key points of research for this project included the experimental demonstration of the new optical excitation technique and an analysis of this technique.

The concept behind the MEMS photocell is based on a very recent line of research that Sandia, and a few other research groups, have developed that explores photo-mechanical interactions [4-6]. In our work, we demonstrated that illuminating specially designed and fabricated nanomechanical resonators with coherent light induces mechanical resonance in the structures. Figure 1 shows a scanning electron micrograph of the nanomechanical resonators and the resulting mechanical response. In our work and the work by other research groups in this area mechanical resonance is generated by having the mechanical structure interact with an optical resonant cavity. This requires that the illuminating light be laser light (i.e. coherent light of a single wavelength).

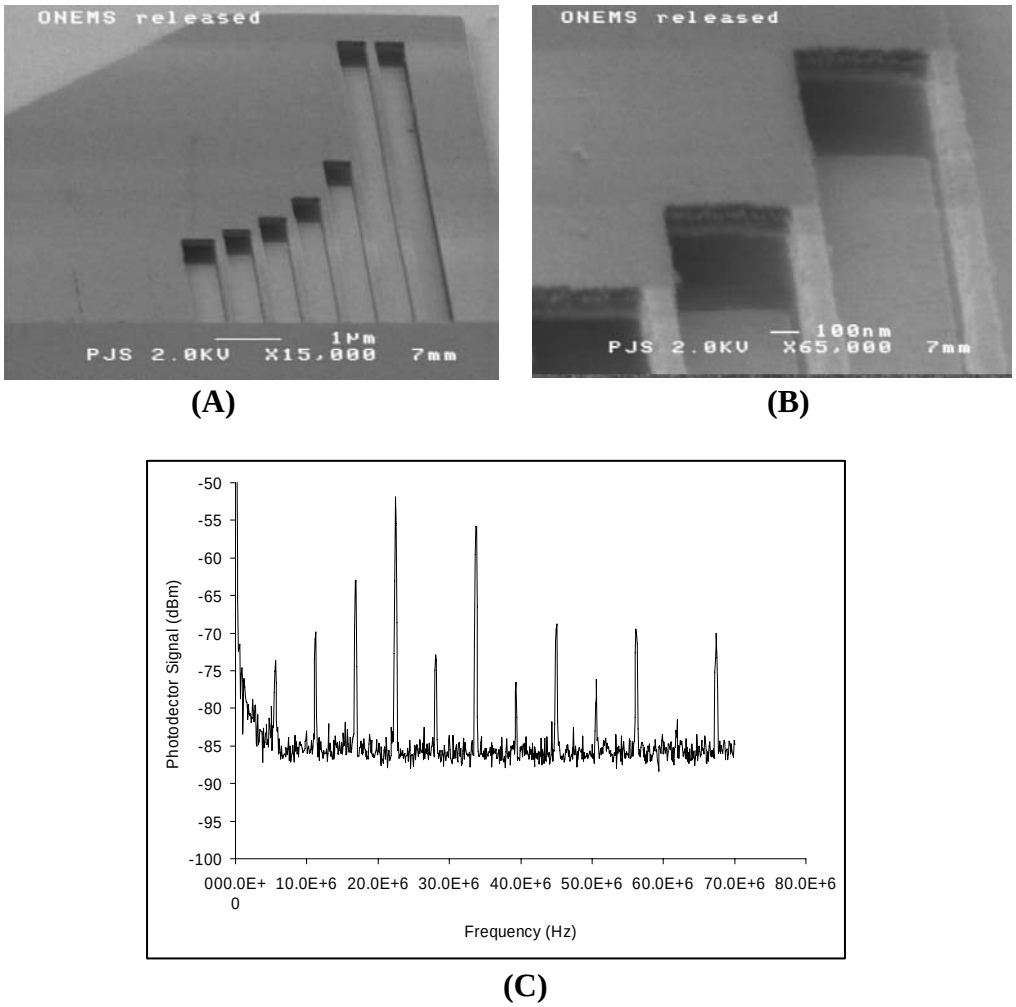

Figure 1 Results from Sandia's optically resonant NEMS work. (A) and (B) show scanning electron micrographs of the NEMS structures. (C) shows the frequency response of the structure when illuminated with coherent light (peaks correspond to excited mechanical modes).

In this project we took advantage of a new technique we devised that allows the use of incoherent/broad-spectrum light (i.e. sunlight) to excite mechanical resonances. To understand the incoherent light approach, it is helpful to understand the coherent light technique. Currently, the MEMS/NEMS devices that have exhibited this optically resonant behavior have a mechanical structure that interacts with an optical cavity. When the mechanical structure displaces, the optical path length of the cavity changes. This change in path length results in a resonant frequency change of the optical cavity. When illuminated with coherent light of a single wavelength, the optical intensity within the cavity changes as the cavity's resonant frequency becomes matched or mismatched to the illuminating wavelength. The intensity of the light in the optical cavity is related to the amount of light that is absorbed in the mechanical structure. Therefore, the temperature of the mechanical structure is dependent on the position of the mechanical structure and the thermal time constant of the structure. If the thermal time constant is roughly matched to the mechanical resonant frequency of the structure, the delay in the thermal domain will correspond to a thermally induced force that is 90° out of phase with the

mechanical displacement of the structure. The result of this optical/thermal/mechanical interaction is resonant mechanical motion.

We can replicate displacement-sensitive temperature dependence in a MEMS structure with incoherent light by creating intensity gradients in the optical field in which the mechanical structure displaces. This can be done by either using an optical aperture or a lens. With an aperture, the mechanical structure would operate at the edge of the optical field (i.e. at the interface of the shadowed and illuminated regions). With the lens, the mechanical structure would operate at the edge of the focal cone. Matching the resonant frequency to the thermal time constant would still apply.

Once the solar energy is converted to mechanical energy, the energy can be readily converted to electrical energy by using either capacitive or piezoelectric energy harvesting techniques. These have already been explored for MEMS devices used for harvesting ambient vibrational energy [2, 3]. Another possibility, depending on the scale of the devices, would be to use the Lorentz law (i.e. the same principle of large scale generators) to generate electricity.

This solar energy conversion technique utilizes a thermal energy conversion process that allows *all* wavelengths to be fully utilized. In PV cells, only the wavelengths that match the band gap energy of the semiconductor are utilized fully for electricity generation (this is the fundamental limit on PV cell efficiencies). If this technique is able to achieve a level of efficiency that is competitive with PV cells (i.e. at least 5-10%), it will offer significant cost savings. The cost savings will come from a direct displacement of the high-cost semiconductor material required for PV cells and possible secondary savings through the elimination of the inverter required in a PV system (the power coming from the mechanical resonant structure would be AC). These two costs alone represent nearly 50% of the costs of current PV power systems.

2.0 MEMS Design and Fabrication

The first prototypes were designed and fabricated using standard MEMS techniques (i.e. using silicon wafers in a traditional semiconductor fab). Future devices could be targeted for low cost production by using glass or other inexpensive substrate materials with low cost MEMS fabrication techniques (e.g. using metals for structural elements with photoresist as the sacrificial material). The devices were designed and fabricated within Sandia's SUMMiT V^{TM} process [7]. This was done primarily for convenience. Future processes optimized for efficiency and cost can be explored in follow-on research.

Due to timing issues, these devices were designed before a thorough analytical exploration of the behavior of these devices could be performed. Therefore, the design of these devices was focused on making a range of devices that would allow flexibility in their testing to provide the most likely demonstration of the effect. In addition, the timing constraints required the design of simple devices so simple cantilever structures were selected for the prototypes.

To achieve device flexibility, a range of cantilevers with different widths and lengths were designed. On each cantilever a series of holes were formed all along the length of the beam. This series of holes was designed to allow the interaction of the light at any position along the length of the beam. Three different hole diameters (5 μm, 7.5 μm, and 10 μm) were used in this series of holes for flexibility in the hole diameter that the light would interact with.

Two basic SUMMiT V^{TM} designs for the cantilevers were used. These designs combined the cantilever with the holes with an underlying, fixed electrode. Both the cantilever and the fixed

electrode were connected with electrical leads to bondpads. This arrangement was used to allow a means of electrical power collection from the device while it was oscillating.

The key difference between the two basic designs was the gap between the cantilever and the fixed electrode. Both varieties utilized the poly4 and metallization layers to create the cantilever. The predominant design in terms of variations provided a gap of about 2 μm. In this case the fixed electrode was built up using poly0, poly1, poly2, and poly3. The other design, of which there was only one variation, had a gap of approximately 10 μm. The bottom electrode in this case is comprised of a laminated poly0 and poly1 structure.

The cantilever was formed out of poly4 and the metallization layer to create a thermal bimorph that would respond mechanically to the variation in temperature resulting from the illumination change with displacement. For this particular device, the metallization layer (aluminum) was decreased from the standard SUMMiT V™ thickness of 700 nm to 100 nm. This was done to reduce the curvature induced by the tensile stress in the aluminum on top of relatively stress free polysilicon structures. The other devices in this particular SUMMiT V™ run were micromirrors that are very sensitive to curvature. However, even with this thin layer of aluminum, the cantilevers did experience some curvature. For the longer cantilevers, this curvature resulted in larger gaps between the cantilever and the fixed electrode at the tip of the cantilever relative to the base. The ultimate effect of this was a reduction in the capacitance of the device. Table 1 shows the design variations implemented in the range of devices fabricated.

Table 1 Device variations fabricated in SUMMiT V™.

Device #	Length (μm)	Width (μm)	Gap (μm)	Aspect Ratio
41	75.0	40.0	2.0	1.88
42	100.0	40.0	2.0	2.50
43	125.0	60.0	2.0	2.08
44	150.0	60.0	2.0	2.50
45	175.0	60.0	2.0	2.92
46	200.0	60.0	2.0	3.33
47	225.0	60.0	2.0	3.75
48	250.0	60.0	2.0	4.17
49	275.0	80.0	2.0	3.44
50	300.0	80.0	2.0	3.75
51	325.0	80.0	2.0	4.06
52	350.0	80.0	2.0	4.38
53	400.0	80.0	2.0	5.00
54	450.0	80.0	2.0	5.63
55	500.0	80.0	2.0	6.25
56	450.0	80.0	10.0	5.63

Figure 2 shows the layout of the SUMMiT V™ module containing the various cantilever devices. Figures 3 and 4 show the layouts of two representative devices. Figure 5 shows an SEM of a representative device.

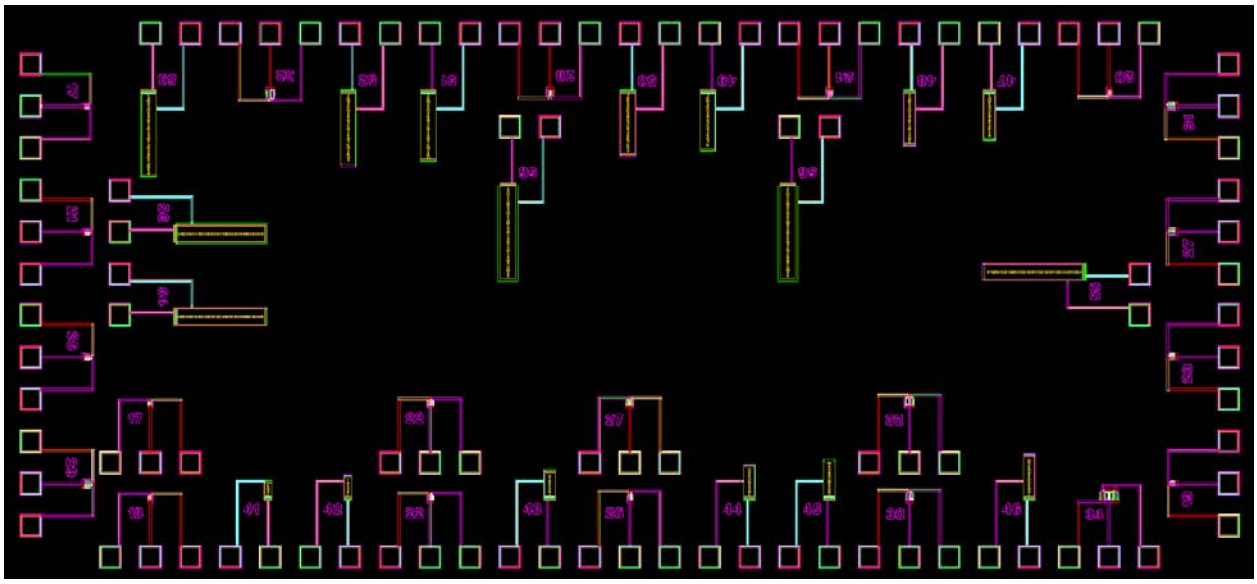

Figure 2 Layout of the SUMMiT V™ module containing the different device design variations. The devices with two bond pads are the cantilever devices. (The devices with three bond pads are micromirrors for another project.)

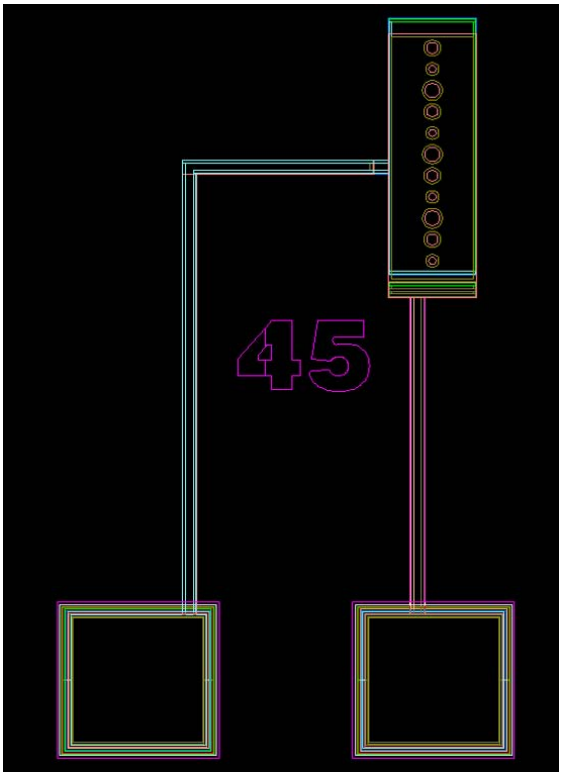

Figure 3 Layout for device 45.

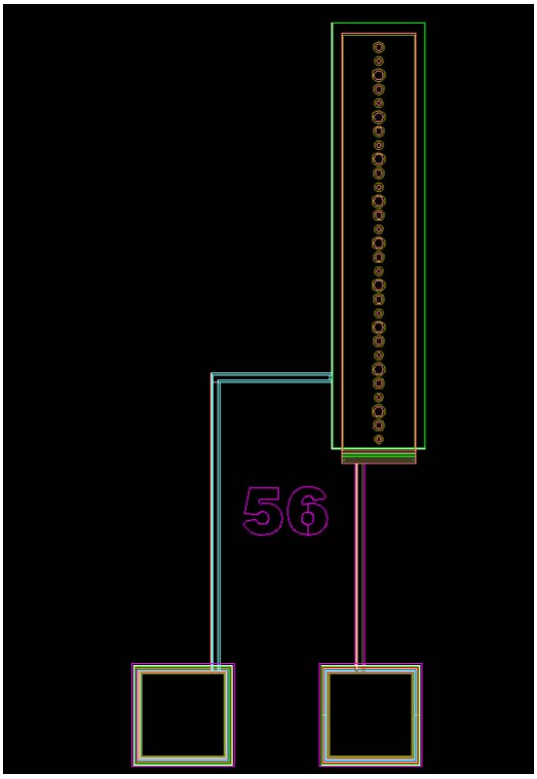

Figure 4 Layout for device 56.

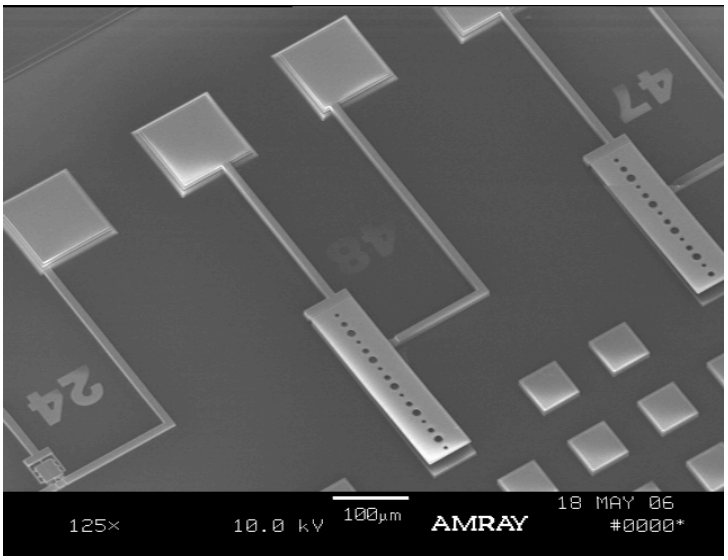

Figure 5 SEM image of cantilever devices, with cantilever 48 shown in its entirety.

3.0 Experimental Results

The goal of the experimental portion of the project was to demonstrate the excitation of a mechanical resonance due to the interaction of the mechanical structure with optical illumination. Of particular interest was demonstrating a new mechanism for light to interact with a mechanical structure to allow the light to excite resonance in the structure without utilizing an optical resonant cavity. This has not been demonstrated before.

3.1 Apparatus and Procedure

The response of the cantilevers to optical illumination was measured experimentally. As shown in the schematic in Figure 6 and pictured in Figure 7, the optical setup had three optical paths for the optical excitation, Polytec laser Doppler vibrometer (LDV), and a CCD camera. For these experiments, the optical excitation source was a 532 nm green laser diode pumped solid state laser with a maximum power of 2.0 Watts. Along the excitation laser path, the light goes through a quarter waveplate (W) followed by a polarizer (P) that are used to regulate the power. Two mirrors (M) turn the laser beam which then goes through a series of lenses (L) and apertures (A) to control the size of the excitation laser spot on the sample and spatially filter the green laser beam. Another mirror turns the green beam towards a dichroic mirror (D2) that reflects the green light towards the sample. When the heating laser is being positioned on a microcantilever, neutral density filters (NDF) are placed between the mirror and D2 such that the green spot will be visible but the power on the microcantilever is small. These filters are removed during data collection.

The green excitation laser goes through a M Plan Apo NIR 20x / 0.40 NA Mitutoyo objective to the sample which is inside a vacuum chamber as pictured in Figure 8. The green laser spot on the upper surface of a microcantilever was around 3-5 μm in diameter. The green laser was focused on the substrate and then moved so that it irradiated the upper surface of a microcantilever. The power of the green laser was monitored between the two mirrors after the polarizer and at the sample. Figure 9 is a plot of the laser power at the sample versus the monitoring location

between the two mirrors, indicating about one-third loss in power. The LDV signal beam exits the fiber through focusing optics. It is turned by a mirror on a gimbaled mount allowing the position of the LDV signal to be altered independently of the green laser location. The LDV light then proceeds through two lenses and a blue-green dichroic plate beam splitter (D1) which transmits the red light. The LDV signal proceeds through the dichroic mirror and objective to the sample, reflects and returns along the same path. In order to image the sample, white light illumination is provided and reflected by the dichroic (D1) towards the sample. Two filters are in front of the camera: one for red light (F1) and one for green (F2).

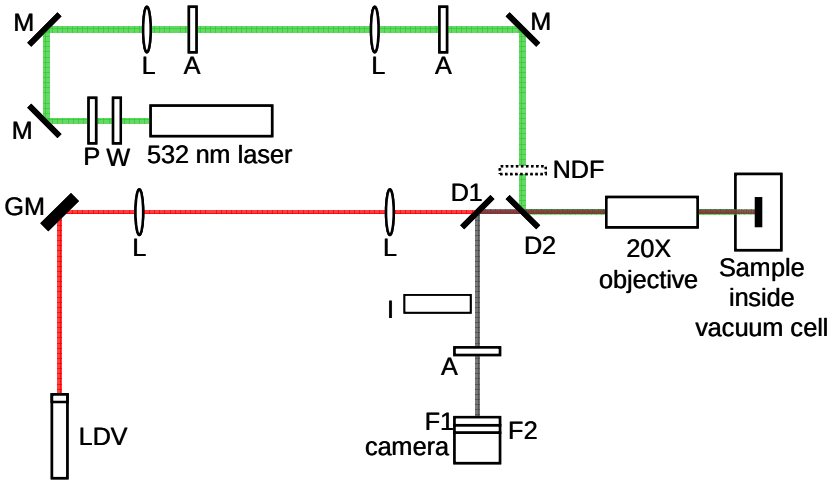

Figure 6 Schematic of the experimental layout.

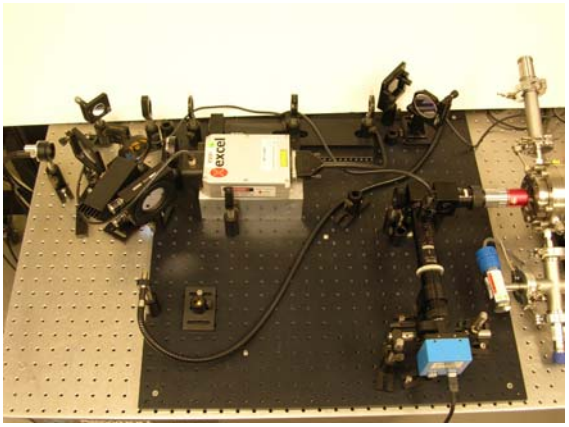

Figure 7 Picture of the experimental layout.

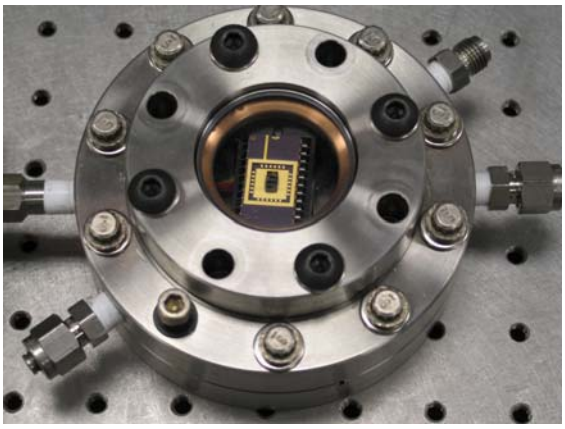

Figure 8 Vacuum chamber with part installed for testing.

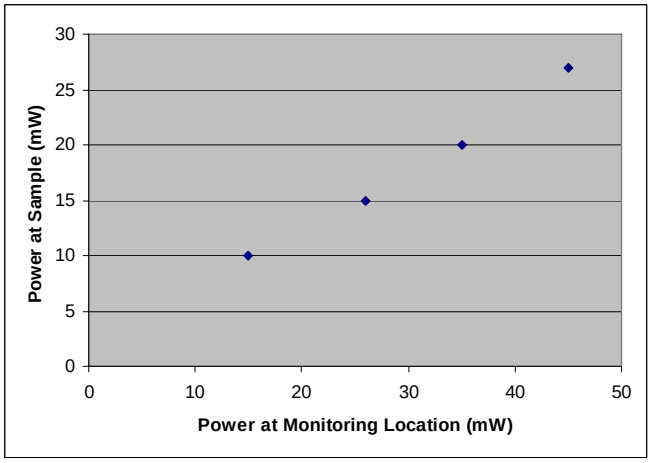

Figure 9 Power of the green excitation at the sample as a function of laser power at the monitoring location between the mirrors.

To increase the sensitivity of the cantilever resonances, all of the testing was done with the parts in vacuum. This increased the effective Q of the cantilevers so that the amplitude of the cantilever resonance was as sensitive as possible to changes in forces acting on the cantilever. The vacuum chamber used, shown in Figure 8, is made from commercially available flange and viewport components stacked together. For the tests reported later, vacuum was maintained below 1 mTorr.

The velocity of the micro cantilevers is measured with a Polytec laser Doppler vibrometer. This instrument uses the frequency shift (Doppler effect) of reflected laser light to measure the velocity of the object from which it is reflected. The output of the LDV is an analog voltage proportional, by a selectable scale factor, to the velocity measured. Its bandwidth is 250 kHz with a minimum detectable velocity of <0.15um/s or 1.5 MHz with a minimum detectable velocity of <0.50 um/s depending on scale factor. When necessary, a Thorlabs DET210 high speed silicon photo detector is used for triggering. The bandwidth on the DET210 is 2.65MHz as it is currently set. Since it is not calibrated, the DET210 was only ever used for triggering data acquisition.

For data collection, an NI PXI-6133 card was used. This provided 8 channels of data acquisition at a maximum rate of 2.5MHz. One of the drawbacks with this card for data acquisition is that it does not have anti-alias filters. This was important for the data reported later since harmonics of the primary cantilever resonant frequencies were almost always present at frequencies above half the highest sample rate. To minimize this effect, most of the data acquired was sampled at the full 2.5 MHz available. A real time display of the LDV response was available during all of the testing and could be paused and saved at any time. Typically, a time history and an averaged spectrum were the desired data.

A typical data collection would begin by putting an ND filter into the high power laser path and removing the 532nm filter in front of the camera. The next step was measuring the laser power output and adjusting the level, accounting for the losses in the optical path, to deliver the desired power to the micro cantilever. With the laser configured this way, the position of the high power laser on the cantilever was visible on the camera and the position was adjusted to the desired location. Next the 532 nm filter for the camera was replaced. At this point the location of the LDV was adjusted with the gimbaled mirror. Typically data were taken with the LDV at one of

the corners at the tip of the cantilever, but this positioning was not strictly controlled introducing some error in the relative magnitudes measured. Once the LDV was correctly positioned, the ND filter was removed from the high power laser path, allowing the full laser power to the cantilever. The real time display of the LDV time history allowed one to check if the optical excitation of the heating laser had successfully excited the resonance of the cantilever. If this had not happened in the initially selected location for the high power laser, the position was modified until the effect was seen. At any time during this process data could be collected from the LDV. In cases where the onset of the phenomenon was to be collected, a card was used in the high power laser path to turn the excitation to the cantilever on or off and the photodiode was used to trigger acquisition.

3.2 Results

The testing can be divided into several parts. The first tests were aimed at verifying that optical excitation induced a mechanical resonance. The next tests were more concentrated on moving the high power laser to various locations and demonstrating that the optical excitation produced a response when the excitation location was varied. The final set of tests conducted was similar to the second set in that various locations were tested, but in this case much more control over the laser focal point was exercised.

The first demonstration of the optical excitation was conducted on cantilever 56. The high power laser spot was not particularly round and only focused to approximately 25 um (based on previous testing, not verified for these tests). Also, the actual focal point of the laser was not known. It may have been significantly above or below the micro cantilever (and likely was since the testing was successful). Figure 10 shows the CCD image of the tip of cantilever 56 showing the high power laser position in green and the LDV position in red. For this test, an arbitrary hole in the cantilever was chosen and the high power laser position was approximately centered on that hole. The high power laser was adjusted to produce 25 mW before injection into the optical path and the LDV measured the velocity of the tip of cantilever 56. For this first set of data, the acquisition rate was 200 kHz. This would prove to be too low to avoid significant aliasing as will be shown shortly.

Figure 10 High power laser and LDV locations for first demonstration of optical excitation.

Baseline data was collected with the cantilevers in vacuum with no high power laser excitation. This is a measurement of the cantilever response to ambient excitation such as Brownian motion, thermal drift, and environmental vibration. It can be used as a baseline for the subsequent analysis of data collected with the high power laser excitation and allows for the identification of

frequencies that have some amplitude but are not associated with the cantilever resonance. Figure 11 shows the average spectrum of this data. Modeling identified 15.3 kHz as the resonance for this cantilever so the peak at 14.2 kHz was attributed to cantilever resonance. The rest of the peaks in the spectrum were attributed to non-structural sources, and it was expected that their amplitudes would stay constant regardless of the cantilever response to the high power laser excitation.

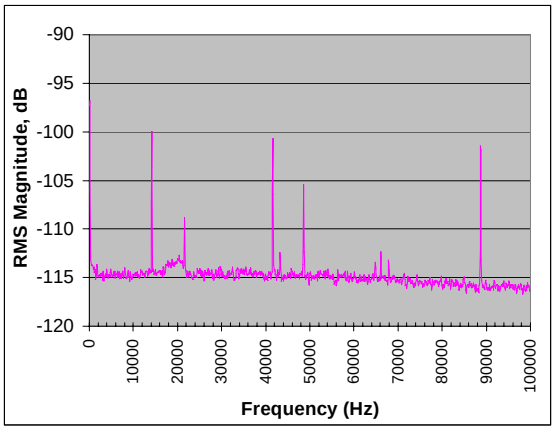

Figure 11 LDV spectrum from tip of cantilever 56 with no high power laser excitation. Cantilever resonance at 14.2 kHz.

The addition of the high power laser excitation produced a significant amplification in the motion of the cantilever at 14.2 kHz. Figure 12 shows the average spectrum recorded with the high power laser excitation and Figure 13 shows a short time history. At the cantilever resonance of 14.2 kHz, the amplitude of the cantilever tip velocity increased by 60 dB (1000x) with the addition of the high power laser excitation. With average peak velocity amplitude of 17 mm/s, that translates into about 191 nm zero-to-peak displacement at the tip of the cantilever. The peaks that look like side lobes on the spectrum plot are all aliased information based on the resonance at 14.2 kHz or harmonics of that frequency. Further tests were all recorded at 2.5 MHz to minimize this.

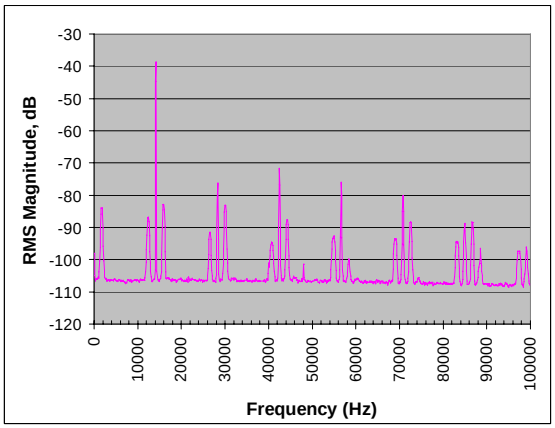

Figure 12 LDV spectrum from tip of cantilever 56 with high power laser excitation. Cantilever resonance at 14.2 kHz with aliasing of harmonics.

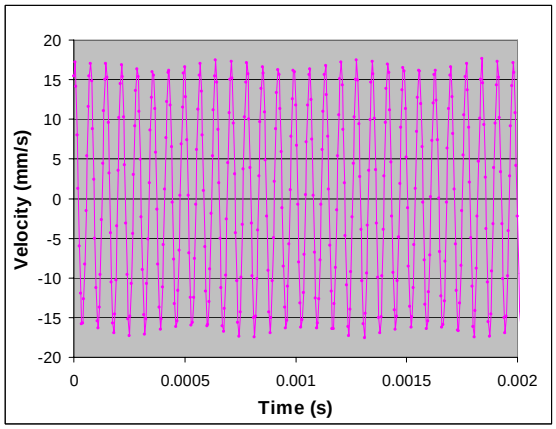

Figure 13 LDV time history from tip of cantilever 56 with high power laser excitation.

The next set of data was collected to demonstrate higher amplitudes of vibration and to see if there was any relationship between hole location and amplitude of vibration. This set of data was from cantilever 48 rather than 56. This cantilever was chosen because it would fit into the field of view on the CCD camera. This allowed the LDV to be repositioned at the tip of the cantilever regardless of where the high power laser was positioned. It was also expected that a shorter cantilever, with less gas damping, would produce higher amplitudes, up to a point. 25 mW of power for the high power laser was used again, and data was collected with it pointed at holes 5, 7, 10, and 14 counted from the root. Figure 14 shows a CCD image of cantilever 48 with the high power laser on hole 10 and the LDV at one corner of the tip.

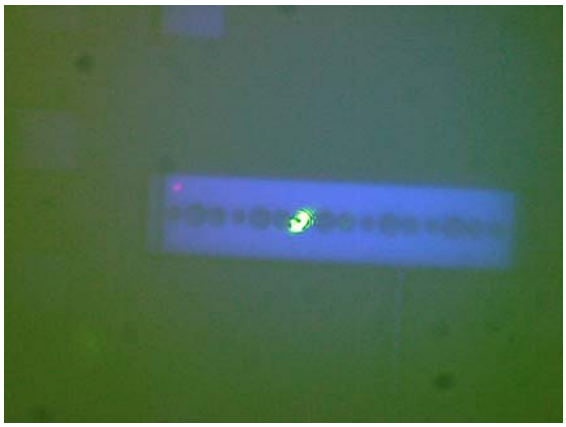

Figure 14 High power laser and LDV locations for second data set of optical excitation effect. Showing 10th hole with LDV in nominal position. (Root on right)

Baseline data was collected prior to adding the high power laser excitation as in the previous test set. Figure 15 shows the average spectrum of this data. Modeling predicted that cantilever 48 would have a first resonance at 50 kHz, so the peak at 45.6 kHz was attributed to structural resonance and the other peaks were attributed to non structural sources.

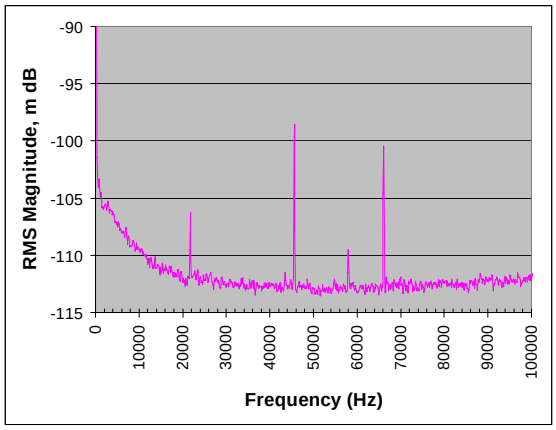

Figure 15 LDV spectrum from tip of cantilever 48 with no high power laser excitation. Cantilever resonance at 50 kHz.

The addition of the high power laser excitation produced a significant amplification in the motion of the cantilever at 45.6 kHz regardless of the hole location. Figure 16 shows the average spectrum recorded with the high power laser excitation for each of the hole locations and Figure

17 shows short time histories. At the cantilever resonance of 45.6 kHz, the amplitude of the cantilever tip velocity increased by up to 80 dB (10000x) with the addition of the high power laser excitation. The average peak velocity amplitude of 205 mm/s for the largest response translates into about 715 nm zero-to-peak displacement at the tip of the cantilever.

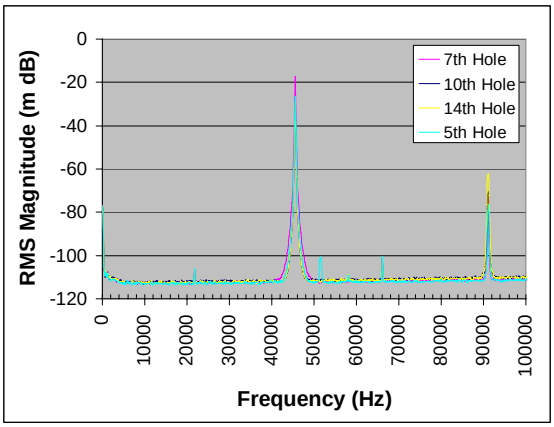

Figure 16 LDV spectrum from tip of cantilever 48 with high power laser excitation. Cantilever resonance at 45.6 kHz.

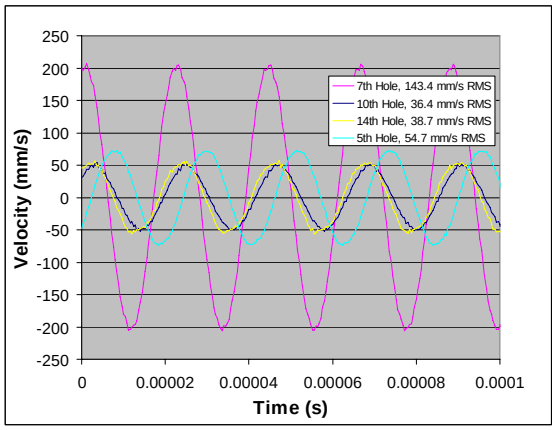

Figure 17 LDV spectrum from tip of cantilever 48 with high power laser excitation.

The amplitude of the response of the cantilever did seem to change with location of the high power laser, but some evidence suggests that the variation was due to instability in the phenomenon rather than hole position. During testing, it was noticed that the amplitude and stability of the optical excitation effect seem to be very sensitive to small changes in position of the high power laser. In fact, a significant amount of time was spent finding just the right location for the high power laser to capture the reasonably stable data presented. Mostly, during testing, the optical excitation phenomenon is unstable and the resonance amplitude changes drastically in a random fashion. Due to this instability in the phenomenon, it seems premature to use the data here as quantitative when comparing high power laser position to cantilever vibration amplitude.

During this test set, the photo diode was used to trigger acquisition in one case with the high power excitation on hole 10 of cantilever 48. The high power laser was still set to 25 mW and the LDV was measuring the cantilever response at the tip. A card was used to block the high power laser and was removed quickly to get a step function for the excitation. The acquisition was triggered on the rising edge of that step. Figure 18 shows the result of this. There is a small response early in the time history that is the static response of the cantilever to the heating from the high power laser. Figure 19 shows a zoomed in view of this static response. The beginning of that static response corresponds to the leading edge of the step excitation from the high power laser. At a much later time, the exponential growth of the vibration response of the cantilever can be seen. This is the response of the cantilever to the parametric excitation.

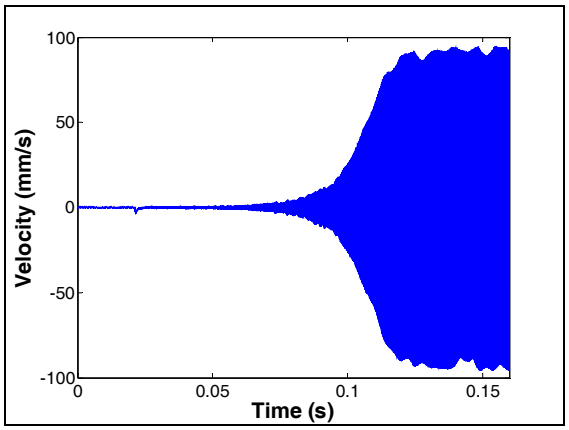

Figure 18 Onset of structural vibration due to parametric excitation on cantilever 48, hole 10.

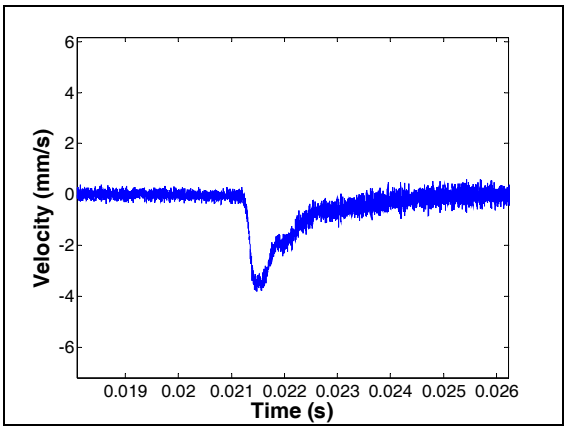

Figure 19 Static portion of the onset of structural vibration due to parametric excitation (Zoomed into 18).

One test of a hole location not originally in the plan showed interesting anomalous results. The high power laser was over hole 9 on cantilever 48 when these results were captured. The cantilever responded with a significantly amplified structural response, but it was at 300 kHz rather than the expected 45.6 kHz. Figure 20 shows the time history captured. Interestingly, the model predicted second bending mode for cantilever 48 is 304 kHz. It appears that the second mode was excited rather than the first.

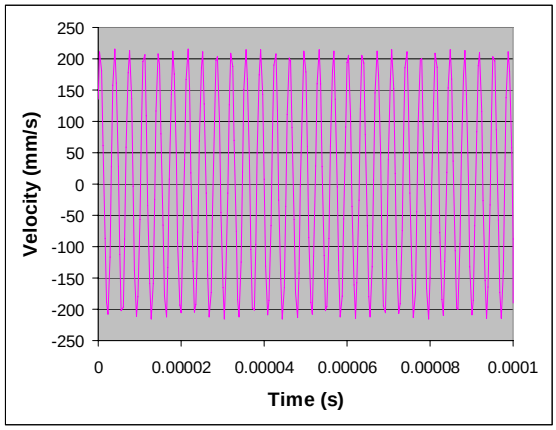

Figure 20 Anomalous result with excitation at hole 9 on cantilever 48.

Additional experiments demonstrated that responses were obtained on cantilever 48 when irradiating all three hole sizes, both near the anchor or tip, on the edge of the cantilever, and on the cantilever itself. Research efforts should be continued to verify the physical phenomena resulting in the response in order to further understand the process and optimize the design. Also, it was shown the minimal amount of excitation laser power at which a parametric excitation occurred was around 5 mW at the monitoring location, corresponding to 3.5 – 4 mW of green laser power incident on the microcantilever.

3.3 Incoherent Light Source Testing

The technique we developed and used to demonstrate optical excitation of mechanical resonance does not use an optical resonant cavity to induce the mechanical resonance. It is the characteristic

that allows us to use this interaction to convert solar energy. While the initial experiments reported earlier all used coherent (i.e. laser) light, we wanted to demonstrate the mechanical resonance using incoherent light. The source needed to mimic solar illumination in that it needed to be from a point source (or provide plane waves). This requirement was difficult to address with sufficient optical power to induce the mechanical oscillations.

We tried two different types of sources. The first source was a standard laboratory white light illumination source. We directed light from that source through a spatial filter to achieve a point source. This attenuated the light to such a degree that there was not sufficient light available to cause resonance.

The next incoherent source we tried was a superluminescent diode. We used a diode that was centered around 680 nm that had a maximum output power of 8 mW. This device also was unable to output sufficient power to cause mechanical resonance. (Much less than 8 mW of power made it to the cantilever device due to the various optical components required in the system.)

Future work in demonstrating the technique with incoherent illumination is a critical step forward. However, finding an adequate power source could be difficult. Possible options include coating the cantilever with an optically absorbing material layer to allow the oscillations to occur at lower power levels, using some other higher-power optical source such as a super-continuum source, or utilizing sunlight for the testing. Each of these options required more time and resources to explore than what we had available for the project.

4.0 MEMS Photocell FEA Simulation and Analysis

A finite element model of the bimorph cantilever beam structure was created to gain intuition into the parameters that affect the performance of the MEMS photocell. This knowledge should lead to improved future designs and an understanding of the energy conversion efficiency of this method.

Figure 21 shows the finite element mesh and the boundary conditions. The heat from the incident light is input as a heat flux, q_{in}, at a point some distance (L_{spot}) from the end of the beam. The device is operated in a vacuum, and the substrate is assumed to be a heat sink, so the other thermal boundary condition is the constant temperature at the anchor point. For convenience, we use T=0 as a reference temperature, so all other temperature results are relative to T=0.

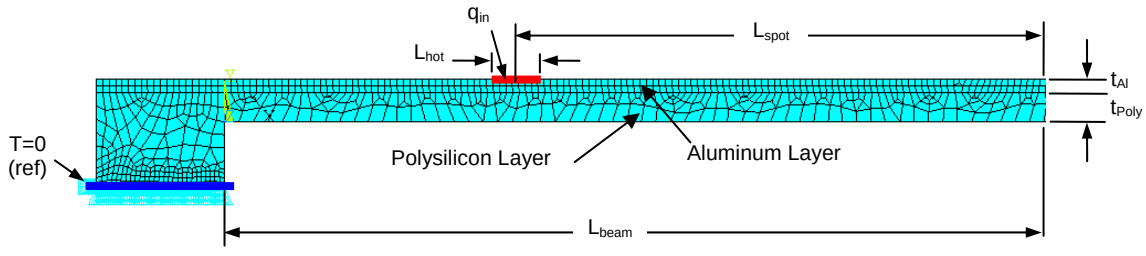

Figure 21 2D finite element model mesh.

4.1 Model Parameters

Table 2 summarizes the nominal input parameters used for the 2D model. Some of these properties are taken from published bulk value parameters for the materials. The structure is

composed of thin films which may introduce different parameters than those used for the model. For instance, the thermal conductivity for the polysilicon is known to be less than the value used in these simulations [8]. The smaller thermal conductivity value will slow the thermal response which, depending on the mechanical response time of the MEMS structure, may either enhance or reduce the optical excitation effect.

Table 2 Nominal thickness and material properties used in the model.

Parameter	Polysilicon	Aluminum	Units
Layer Thickness	2.25	0.1	μm
Young's Modulus	164000	70000	MPa
Density	2.331e-9	2.697e-9	$mg/\mu m^3$
Poisson Ratio	0.23	0.33	
Coefficient of Thermal Expansion	2.8e-6	23.1e-6	μm/μm-K
Thermal Conductivity	148e3	237e3	nW/μm-K
Specific Heat Capacity	712e6	903e6	pJ/mg-K

4.2 Modal Analysis

Obtaining the natural frequency of the cantilever beams is one way to experimentally validate the structural model. Figure 22 shows the mode shapes from a modal analysis of the model. For device 48, the frequencies for the first two modes were predicted to be 48.5 kHz and 303.9 kHz. For device 56, the frequencies for the first two modes were predicted to be 15.04 kHz and 94.3 kHz. These were close to the measured values of 14.16 kHz and 45.63 kHz for devices 56 and 48, respectively. In both cases, the model is over-predicting the frequency by about 6%.

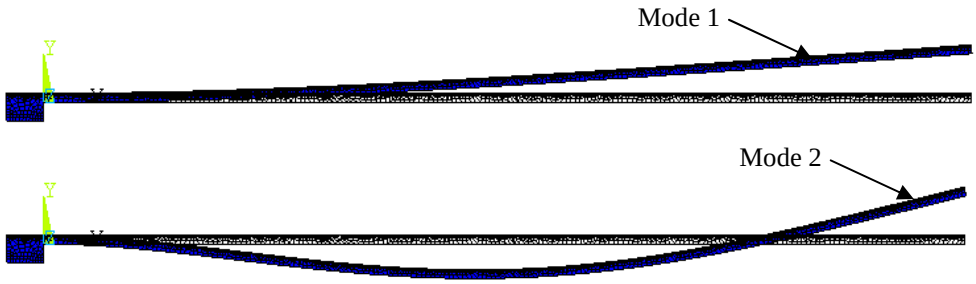

Figure 22 Mode shapes for the first and second modes.

To determine the effect of the holes in the actual beams, another model was developed using layered shell elements. Without holes, the natural frequency of device 56 was 15.16 kHz. With the holes, shown in Figure 23, the frequency was 14.95 kHz. The natural frequency for device 48 without holes was 49.02 kHz and with holes was 48.32 kHz. These results indicate that the presence of the holes has little effect on the natural frequency, so the difference between the model and experimental results is likely due to other effects. The frequency is sensitive to the thickness and stiffness of the polysilicon and aluminum layers, so uncertainty in these parameters could account for some of the difference between the model and the experiment.

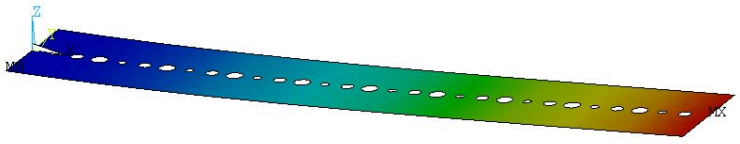

Figure 23 Mode shapes for device 56 using layered shell elements. Color gradient shows deflection out of plane (in the z-direction).

4.3 Optical Model: Input Power for the Thermal Model

The thermal model is based on knowing the power P_{in} absorbed by the beam. Because the model is 2D, the input to the model is the power per unit width, or $p_{in}=P_{in}/w$ where w is the width of the beam. The boundary condition is an applied heat flux, or $q_{in}=p_{in}/L_{hot}$, where L_{hot} is the length of the heated region (shown in Figure 21). L_{hot} is calculated by dividing the actual heated area (πr_{spot}^2) by the width of the beam, where r_{spot} is the radius of the incident light. As the beam moves out of plane, the heated region will change in size, and due to the interaction with the hole, the absorbed power will vary. The heated region is small compared to the size of the beam, so we simplify the model by keeping the heated region a fixed size. To account for the change in absorbed power, the heat flux is varied based on the displacement and the light characteristics. To calculate the power absorbed by the light, we use the equations for the power lost by a Gaussian beam passing through an aperture.

For a laser with a total transmitted power of P_0 passing through the center of a hole of radius r in the cantilever, the power absorbed by the cantilever is given by

$$P_{in} = \eta_{abs} P_0 e^{-2r^2/w^2(z)}$$

$$w(z) = w_0 \sqrt{1 + \left(z / z_r\right)^2}$$

$$z_r = \frac{\pi w_0^2}{\lambda}$$

where w_0 is the waist radius of the beam, z_r is the Rayleigh range, λ is the wavelength of the beam, z is the distance from the waist radius along the length of the beam, and η_{abs} is percent of incident light absorbed due to reflectivity and the absorption properties of the material. These equations are used directly within the finite element model, and the out-of-plane displacement at the location L_{spot} is what determines the variation in z that leads to parametric excitation.

For the analysis, we will use the values given in Table 3 for the laser beam. Note that the location of the initial spot ($z_{initial}$) is obtained by focusing the laser at the distance $z_{initial}$ *below* the beam. The value for z is obtained by $z=z_{initial}+\delta y_{spot}$, where δy_{spot} is the displacement of the cantilever beam at L_{spot}. As the beam is heated, δy_{spot} becomes increasingly negative, so if the laser is focused *below* the cantilever, $w(z)$ will approach w_0 as the cantilever is heated.

Table 3 Nominal beam parameters used for analysis.

Parameter	Value	Units
Beam Waist Radius (w_0)	2	μm
Optical Wavelength	0.633	μm
Radius of Hole	2.5	μm
Location of Initial Spot ($z_{initial}$)	25	μm

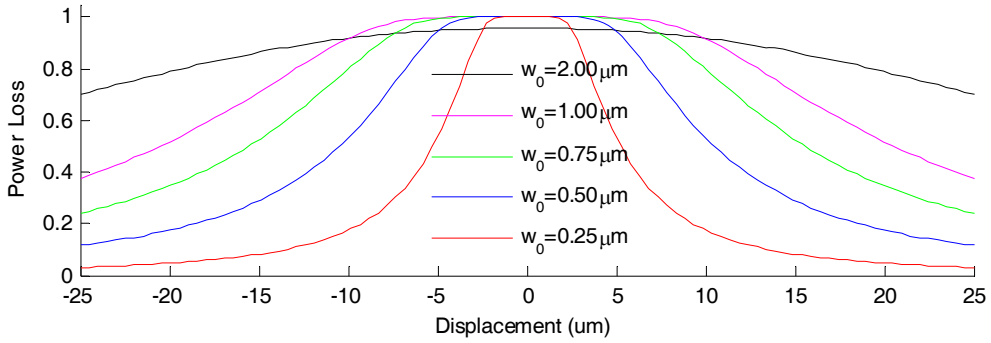

Figure 24 Power loss vs. displacement.

Figure 24 shows the power loss, in percent, through an aperture of 2 µm for beams with different apertures or waist radii as a function of the displacement of the beam along the axis of the laser where the initial position of the beam is at $z_{initial}$=0. If the peak-to-peak oscillation of the cantilever is less than 5 µm, then the initial position of the beam should actually be located some distance z from the beam focus. For example, if w_0=0.25µm, $z_{initial}$ should be about 5 µm. The larger the slope of the power loss vs. displacement, the more variation there will be in the heat flux vs. displacement, which should result in a larger amplitude of oscillation.

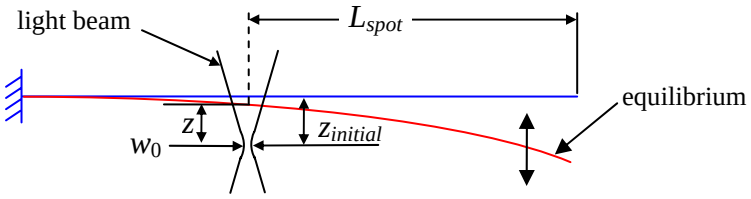

Figure 25 Schematic showing beam.

The value for $z_{initial}$ should also be chosen based upon the deflection of the beam at equilibrium. If the desire is to have a large slope at the point of equilibrium, then the value of $z_{initial}$ should be the point of largest slope plus the displacement of the beam at equilibrium (see Figure 25).

There may be a trade-off between the amount of power absorbed vs. the slope of the curve, because the displacement is also a function of the temperature, and changing $z_{initial}$ changes the power loss. That is something worth investigating in the future.

4.4 Thermal Equilibrium

When you turn on the laser, there will be a transient effect while the beam reaches its equilibrium temperature and displacement. A quasi-static analysis can be performed to determine the relationship between the input power, spot location, and displacement. To reduce the solution time (due to requiring less elements), we will use an Aluminum thickness of 1.0 µm and refer to this theoretical device as 48A1.

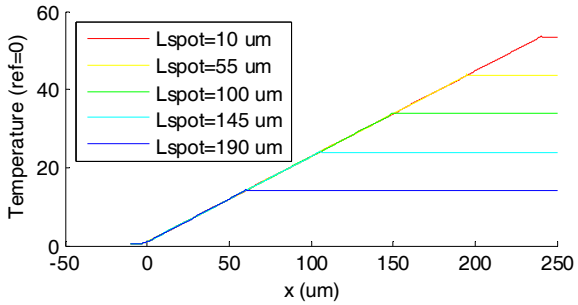

Figure 26 Equilibrium temperature along the top surface of the beam for the P_0=25 mW.

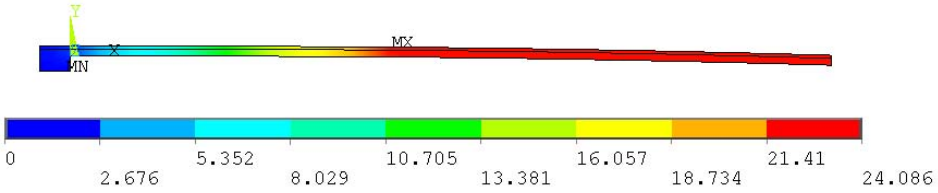

Figure 27 Temperature profile of beam for L_{spot} = 145 µm.

To account for the interaction of the laser with the hole in the cantilever, the analysis can be done in two or three steps to couple the optical and thermal-mechanical models. For example, for the beam focused at a L_{spot} = 145 µm, a power of P_0=25 mW, and η_{abs}=100%, and an Aluminum thickness of 1.0 µm, the deflection of the tip of the beam at equilibrium after the first iteration is -2.9954 µm. Updating the heat flux results in a second iteration of -2.9429 µm and updating a third time gives -2.9438 µm. The amount of power actually absorbed, using the beam characteristics from Table 3, is about 7.34 mW or 29.4%. Figure 28 shows how the absorbed power and tip displacement at equilibrium vary versus hole location for the same beam characteristics.

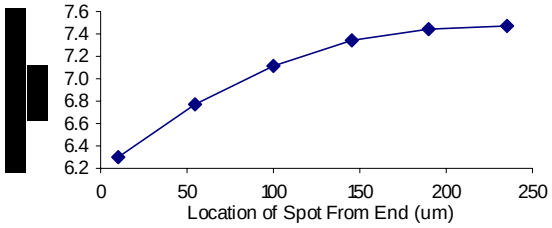

(a)

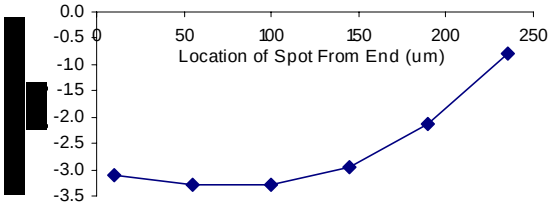

(b)

Figure 28 (a) Power absorbed and (b) Tip displacement vs. distance of hole from end of cantilever for device 48A1 and beam characteristics given in Table 3.

4.5 Thermal Time Constant

The driving force that causes the beam to oscillate is the variation in the heat flux, $q(z)$, as the beam displaces. This is essentially a feedback mechanism in which a certain amount of energy is input into the beam each cycle. For the beam to resonate at some amplitude, the incremental energy injected during each cycle must be at least equal to the energy lost due to damping. The damping can be in the form of material damping, thermal damping, electrostatic damping (i.e. electrically removing energy from the system), or squeezed-film damping. The device operates in a vacuum, so we will neglect squeezed-film damping. The material damping was determined by measuring the quality factor of the cantilever beams oscillating in a vacuum. The quality factor (Q) was found to be about 40,000.

Although there may be a large variation in heat flux with displacement, one can think of the heat transfer as contributing to thermal damping. This can be taken into account in the finite element model when performing a transient (time-dependent) analysis. For design purposes, we can perform an analysis in which the heat flux is held constant. Figure 29 shows the response of device 48A1.

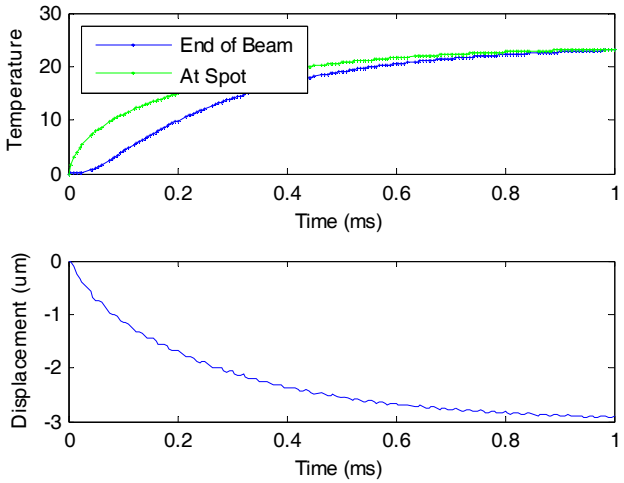

Figure 29 Transient response of device 48A1 after laser is turned on (L_{spot} = 145 μm).

The oscillation in the displacement observed in Figure 29 is caused by the sudden onset of the heat flux (i.e. thermal impact). The expansion of the material and difference in CTE of the two materials causes an internal moment in the beam that eventually becomes a distributed moment along the beam. The moment is a function of the temperature at that point on the beam and the temperature is a function of time. If over time the moment increases too slowly, the effect is quasi-static and the beam will reach equilibrium without oscillating.

The thermal time constant is highly dependent on the location of the laser (L_{spot}). Figure 30 shows the response for the case where the spot is near the end of the cantilever. There are no oscillations in the displacement – although when printed or viewed on-screen, there may appear to be very small oscillations in Figure 30. The thermal time constant for device 48A1 is approximately 0.23 ms for L_{spot} = 10. This is an order of magnitude larger than the period of mechanical oscillation (0.0176 ms, or f=56.5 kHz).

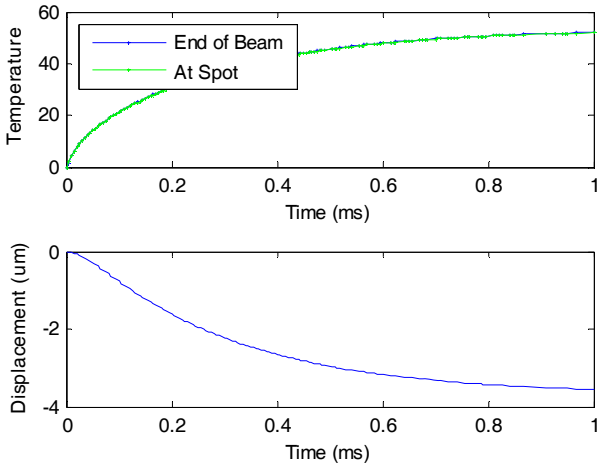

Figure 30 Transient response of device 48A1 after laser is turned on (L_{spot} = 10 μm).

From the experimental results, when the laser it turned on, the cantilever takes about 2-4 ms to overcome the initial transient and reach the equilibrium displacement. This is on the same order of magnitude as predicted with the model. (Keep in mind that some results shown here are for 48A1 as opposed to a model of the actual thickness.)

When the laser is not at the end of the beam, there is a question about whether the thermal time constant for the device should be calculated as the time it takes for the temperature at the spot to reach 63% of the final temperature. That is because the rate of change in temperature at L_{spot} is different than the rate of change at the tip of the beam. It may be more reasonable to think of the case where the cantilever beam has a length of $L = L_{beam}$-L_{spot} and the end of the beam is at a constant temperature and thermally insulated from the rest of the beam.

For example, to calculate the thermal time constant of device 48A1 when the laser is at L_{spot} = 145 μm, we evaluate the thermal time constant for the case where L = 95 μm. The result is a thermal time constant of 0.042 ms. This value is much closer to the mechanical time constant, which explains why we see the oscillation of the beam in Figure 29. If L = 50 μm, the thermal time constant is 0.014 ms.

The model can be used to investigate how the thermal time constant changes when other design parameters, such as thickness and width, are modified. The thickness affects both the heat transfer and the natural frequency, so little is to be gained by changing thickness. The width of the cantilever does not affect the natural frequency or the thermal time constant, but it does affect how much power is required to heat the beam to a given temperature. Therefore, the efficiency might be improved by reducing the width of the beam. Increasing the density of the material lowers the natural frequency. Decreasing the heat capacity decreases the thermal time constant. Reducing the stiffness of the beam decreases the natural frequency. Modifying the relative stiffnesses and coefficients of thermal expansion of the bimorph materials can effect the displacement at a given temperature.

More work is needed to determine how to most appropriately match the thermal time constant to the mechanical frequency in order to achieve the highest amplitude of oscillation and efficiency. Additional modeling, sensitivity analysis, and optimization would be useful.

4.6 Transient Model for Simulating Excitation

Coupling the optical, thermal, and mechanical models in a transient solution requires calculating the new heat flux at each time step based on the current deflection. Because of the inability within the software to converge at each step, the time step must be very small to avoid numerical error. The amplitude of oscillation appears to be highly dependent on the time step, without significant convergence even at 80 steps per period.

Both the experimental results and the modeling show that it takes a large number of cycles to reach the limit-state. The experimental results show it taking about 100 ms to reach the limit state. For a period of 0.042 ms, that is about 2830 cycles, or 95200 time steps (at 40 steps per cycle). Each time step takes about 1.25 seconds, so the analysis would take about 33 hours.

Using the properties and values given in Tables 2 and 3, the model would not resonate. So, we changed the beam waist radius to w_0=0.25 µm and the initial offset to $z_{initial}$=6 µm. Figures 31-34 show the results obtained from the transient model for L_{spot}=145 µm.

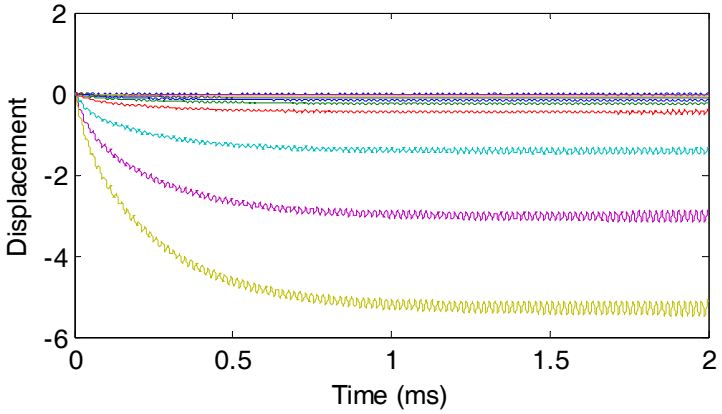

Figure 31 Displacement vs. time at multiple points along the beam.

Figure 31 shows that the amplitude of oscillation is increasing. Due to time constraints, we were unable to run the model for the entire 33 hours. Instead, we ran simulations in which we first solved for the displacement at equilibrium using a quasi-static analysis. Then we added a displacement constraint at the end of the beam that represents the estimated maximum amplitude of the oscillation. Then we began the transient solution and removed the displacement constraint.

Figure 32 shows the results for an initial amplitude of ±2.0µm. Note that the amplitude of oscillation is increasing. Without damping and nonlinearities, we'd expect this amplitude to continue to increase. If we increase the material damping to the point where the amplitude no longer increases, we may be able to use that amplitude as a means of comparing other designs.

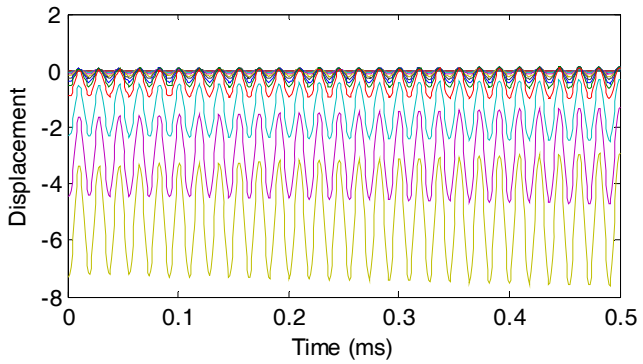

Figure 32 Displacement vs. time at multiple points along the beam for an initial amplitude of ±2.0 µm, *Q* = 40,000.

The quality factor at which the amplitude no longer increased for an initial specified amplitude of ±4 µm was between 100 and 1000 (see Figures 33 and 34). This approach is much more efficient than running the model starting from when the laser is turned on. However, more work is needed to verify that the two methods converge to the same steady-state amplitude.

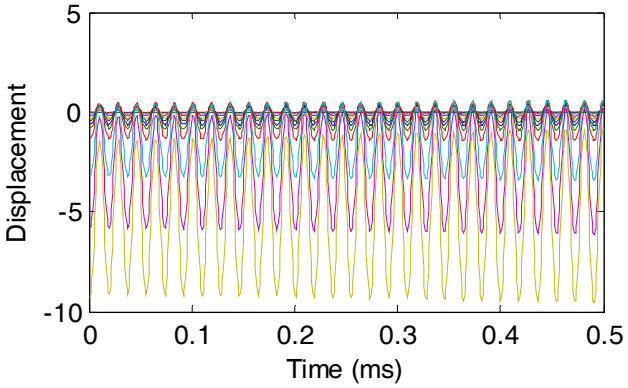

Figure 33 Displacement vs. time at multiple points along the beam for an initial amplitude of ±4.0 µm, *Q* = 1,000.

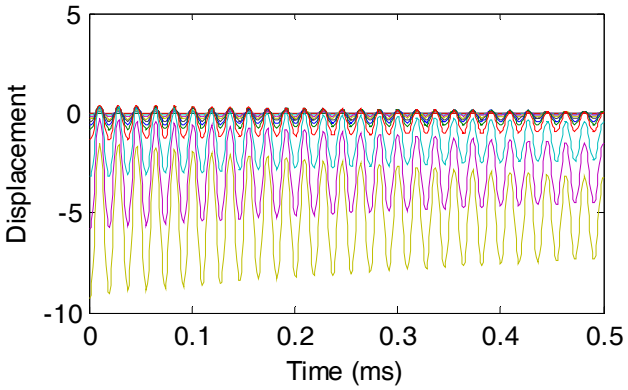

Figure 34 Displacement vs. time at multiple points along the beam for an initial amplitude of ±4.0 µm, *Q* = 100.

Without validation or error analysis, we cannot say for sure whether the transient model is accurately showing the effect of the varying heat flux. We do know that the amplitude of

oscillation is affected by the size of the time step, so that needs to be investigated further. More analysis and experimental validation would be required to gain confidence that the transient model is providing realistic results.

4.7 Design Trade-offs

The main tradeoffs with the cantilever beam design are (1) we need large motion to get a large change in heat flux and (2) we need a small thermal time constant to avoid thermal damping. There may be other approaches to reducing the thermal time constant other than changing the location of the laser, but we did not find any significant enough to reduce the time constant a whole order of magnitude. The problem with moving the location of the spot closer to the anchor is that (1) more heat is lost to the substrate (2) the temperature is lower and therefore the overall displacement of the cantilever is lower, and most importantly (3) the displacement at the spot decreases as you move closer to the anchor.

5.0 Summary and Future Work

In this project we have devised and demonstrated a new optical technique to induce mechanical resonance in a MEMS cantilever. This technique is particularly interesting due to it being able to work with either coherent or incoherent light. It does require that the light be from a point source or be a plane wave. This unique aspect of the device allows it to use sunlight to induce mechanical vibrations which can in turn be converted to electrical power through piezoelectric or capacitive vibrational energy harvesting techniques [1, 2].

We have experimentally demonstrated inducing mechanical resonance in a MEMS structure using this new technique with coherent light. We have also modeled the effect using finite element analysis. Both efforts have given some insight into how to maximize the efficiency of the device. However, the insight is primarily qualitative and further work needs to be done to move this from being a unique demonstration to being something understood well enough to use for solar energy harvesting or in some other system.

Some areas of further experimental research include:

- Demonstrating excitation of mechanical resonance using an incoherent light source.
- Utilizing capacitive or piezoelectric effects to monitor performance and extract power from the vibrating mechanical structure.
- Achieving consistent results such that comparison with simulations and analytical models is possible.

Areas of further research in analysis and design:

- Develop a model (FEA or analytical) that provides an accurate estimate of the energy conversion efficiency of this technique.
- Optimize the design of the structure to evaluate the realizable energy conversion efficiency of this structure.

References

1. **Nielson, G. N. and Watts, M. R., *Exciting Mechanical Resonance through Incoherent Optical Illumination*, Sandia National Laboratories Technical Advance, 2005.**
2. **Parton, E., T. Sterken, and Fiorini, P., "A new MEMS design for the recovery of natural vibration," *Elettronica Oggi*, 346, p. 44-47, 2005.**
3. **Jeon, Y. B., Sood, R., Jeong, J.-h., and Kim, S. G., "MEMS power generator with transverse mode thin film PZT," *Sensors and Actuators A (Physical)*, 122, p. 16-22, 2005.**
4. **Rokhsari, H., Kippenberg, T. J., Carmon, T., and Vahala, K. J., "Radiation-pressure-driven micro-mechanical oscillator," *Optics Express*, 13, p. 5293-5301, 2005.**
5. **Aubin, K., Zalalutdinov, M., Tuncay, A., Reichenbach, R. B., Rand, R., Zehnder, A., Parpia, J., and Craighead, H., "Limit cycle oscillations in CW laser-driven NEMS," Journal of Microelectromechanical Systems (JMEMS), 13, p. 1018-1026, 2004.**
6. **Metzger, C.H. and Karrai, K., "Cavity cooling of a microlever," *Nature*, 432, p. 1002-1005, 2004.**
7. ***Sandia MEMS Advanced Design Short Course*, Class Materials, 2004.**
8. **Phinney, L. M., Kuppers , J. D., and Clemens, R. C., *Thermal Conductivity Measurements of SUMMiT^{TM} V Polycrystalline Silicon*, Sandia Report SAND2006-7112, November 2006.**

Distribution List

1	MS1070	David S. Epp	01526	(electronic copy)
1	MS1110	Vipin P. Gupta	06337	(electronic copy)
1	MS0982	Uma Krishnamoorthy	05765	(electronic copy)
1	MS1080	Gregory N. Nielson	017492	(electronic copy)
1	MS0346	Leslie M. Phinney	01514	(electronic copy)
1	MS1069	Jonathan W. Wittwer	017491	(electronic copy)
1	MS1080	Keith Ortiz	01749	(electronic copy)
1	MS1069	Mark R. Platzbecker	017491	(electronic copy)
1	MS1077	Thomas E. Zipperian	01740	(electronic copy)
1	MS1110	Jeffrey S. Nelson	06337	(electronic copy)
1	MS0346	Daniel J. Rader	01513	(electronic copy)
1	MS0372	James M. Redmond	01525	(electronic copy)
1	MS0824	Tze Yao Chu	01500	(electronic copy)
1	MS0346	Justin R. Serrano	01513	(electronic copy)
1	MS9004	William P. Ballard	08100	(electronic copy)
1	MS9292	Joseph S. Schoeniger	08321	(electronic copy)
1	MS1070	C. Channy Wong	01526	(electronic copy)
1	MS0847	Peter J. Wilson	01520	(electronic copy)
1	MS0899	Technical Library	09536	(electronic copy)
1	MS0123	Donna L. Chavez	01011	(electronic copy)

Sandia National Laboratories